Electronic Supplementary Material (ESI) for Inorganic Chemistry Frontiers.

Supporting Information

Design of fluorine substituted high-entropy phosphates as cathode materials towards high-performance Na-ion batteries

Qi Wang [a], Man Zhao [a], Hai-tao Yu [a], Ying Xie [a,b,*], Ting-Feng Yi [b,c,*]

[a] *Key Laboratory of Functional Inorganic Material Chemistry, Ministry of Education, School of Chemistry and Materials Science, Heilongjiang University, Harbin, 150080, PR China*

[b] *Key Laboratory of Dielectric and Electrolyte Functional Material Hebei Province, School of Resources and Materials, Northeastern University at Qinhuangdao, Qinhuangdao 066004, PR China*

[c] *School of Materials Science and Engineering, Northeastern University, Shenyang, 110819, PR China*

*Corresponding author: Ying Xie

E-mail: xieying@hlju.edu.cn (Dr. Ying Xie).

*Corresponding author: Ting-feng Yi

E-mail: tfyihit@163.com

1. Material characterisation

The crystal structures of the samples were analysed by X-ray powder diffractometer (XRD, Bruker D8, Cu-Kα, λ = 1.54056Å) in the range of 10-80° (2θ). Sample morphology and microstructure were observed using a scanning electron microscope (SEM, Hitachi S-800) and a transmission electron microscope (TEM, JEOL-2100). Electron diffraction images were obtained by fast Fourier transform (FTT). Chemical bonds were analysed using a Fourier infrared absorption spectrometer (FT-IR, Thermo Scientific Nicolet iS10). And particle size was determined using a particle size analyser (Nano-ZS90, Malvern). Elemental distribution was determined using an energy spectrometer (EDS, Oxford INCA, British). X-ray photoelectron spectroscopy (XPS) was performed using an ESCA Lab 250 system.

2. Electrochemical characterisation

The electrochemical tests of the prepared samples were all carried out in a half-cell, where the active material, conductive carbon black and polyvinylidene fluoride were mixed in a mass ratio of 8:1:1 and dissolved in N-methyl -2-pyrrolidone (NMP) to form a slurry. This slurry was uniformly coated on aluminum foil and dried in a vacuum oven at 110 °C for 11 h. Circular electrode sheets with a diameter of 14 mm were prepared, and the loading of active material on each electrode was in the range of 1.2-1.4 $mg\cdot cm^{-2}$. Sodium metal was chosen as the anode material, and glass fiber filters (Whatman) were used as the septum. The electrolyte consisted of 1 M $NaClO_4$, propylene carbonate (PC) and 5 vol% solution of fluoroethylene carbonate (FEC). The final assembly of the

CR2025 button cell was carried out in a glove box filled with argon gas. The tests were carried out at room temperature (≈25 °C) and the electrochemical performance of the half-cells was tested at different current densities using a CT-4008 T system in the voltage range of 1.5-4.5 V. The electrochemical performance of the half-cells was measured using a CT-4008 T system. Cyclic voltammetry (CV) tests were performed at different scan rates using a CHI1000C electrochemical workstation. Electrochemical impedance spectroscopy (EIS) tests were performed using a Princeton P4000 electrochemical work in the frequency range of 0.01 Hz-100 kHz with a constant potential signal amplitude of 5 mV.

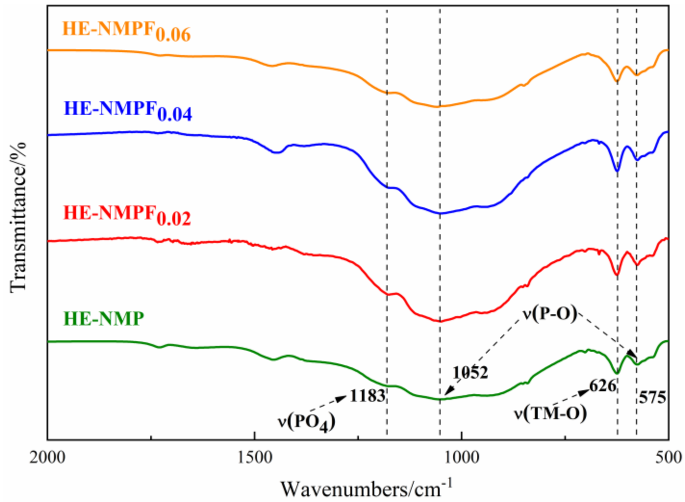

Fig. S1 Fourier transform infrared (FT-IR) spectrum of the different samples.

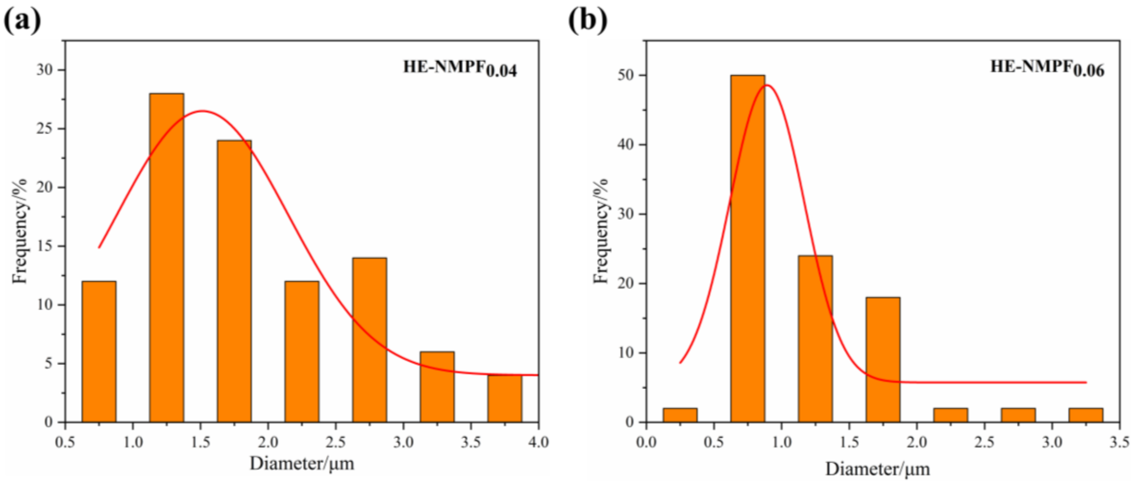

Fig. S2 Particle size distdibution histogram of (a) HE-NMPF$_{0.04}$ and (b) HE-NMPF$_{0.06}$.

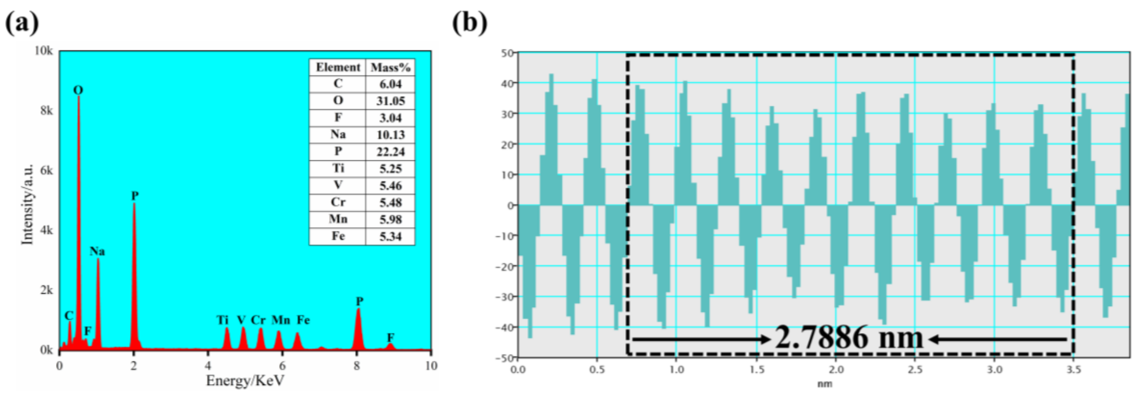

Fig. S3 (a) Energy Dispersive Spectroscopy (EDS) pattern and (b) the contrast curves indicate the interplanar space of the HE-NMPF$_{0.02}$.

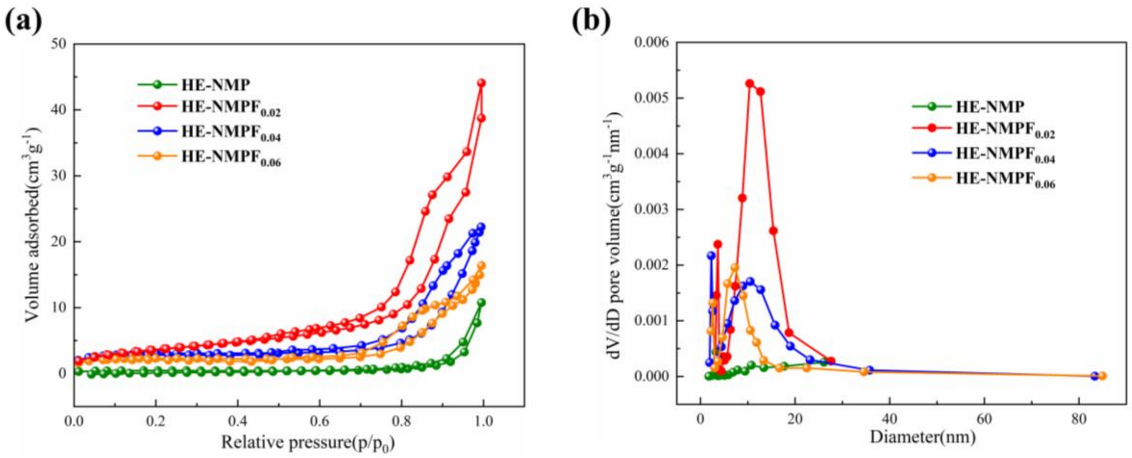

Fig. S4 (a) N_2 adsorption-desorption isotherms and (b) pore size distributions of different samples.

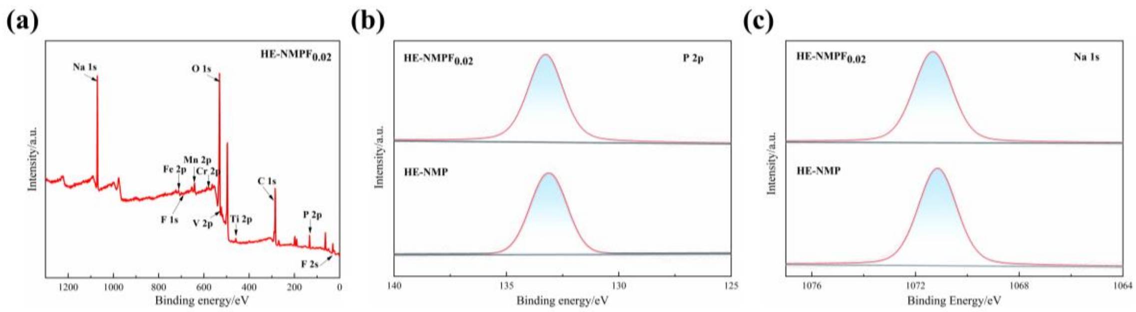

Fig. S5 (a) XPS full spectrum of the HE-$NMPF_{0.02}$, (b) P 2p, (c) Na 1s XPS spectra of HE-NMP and HE-$NMPF_{0.02}$.

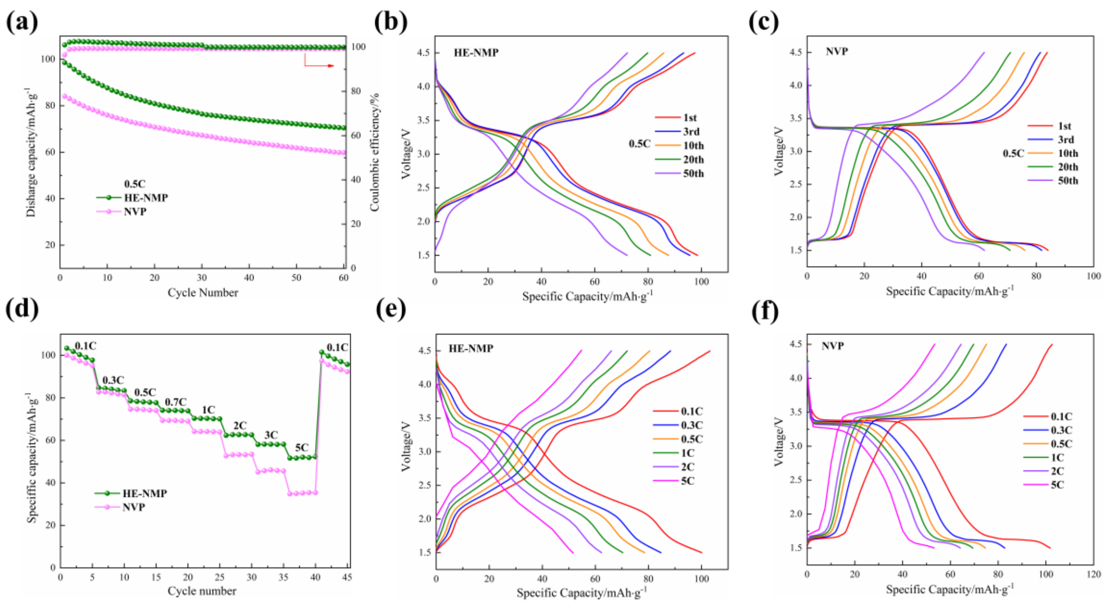

Fig. S6 (a) Cycling performance of different samples; Charge/discharge curves of (b) HE-NMP and (c) NVP at 0.5 C; (d) Rate performance; Charge/discharge curves of (e) HE-NMP and (f) NVP at different current density.

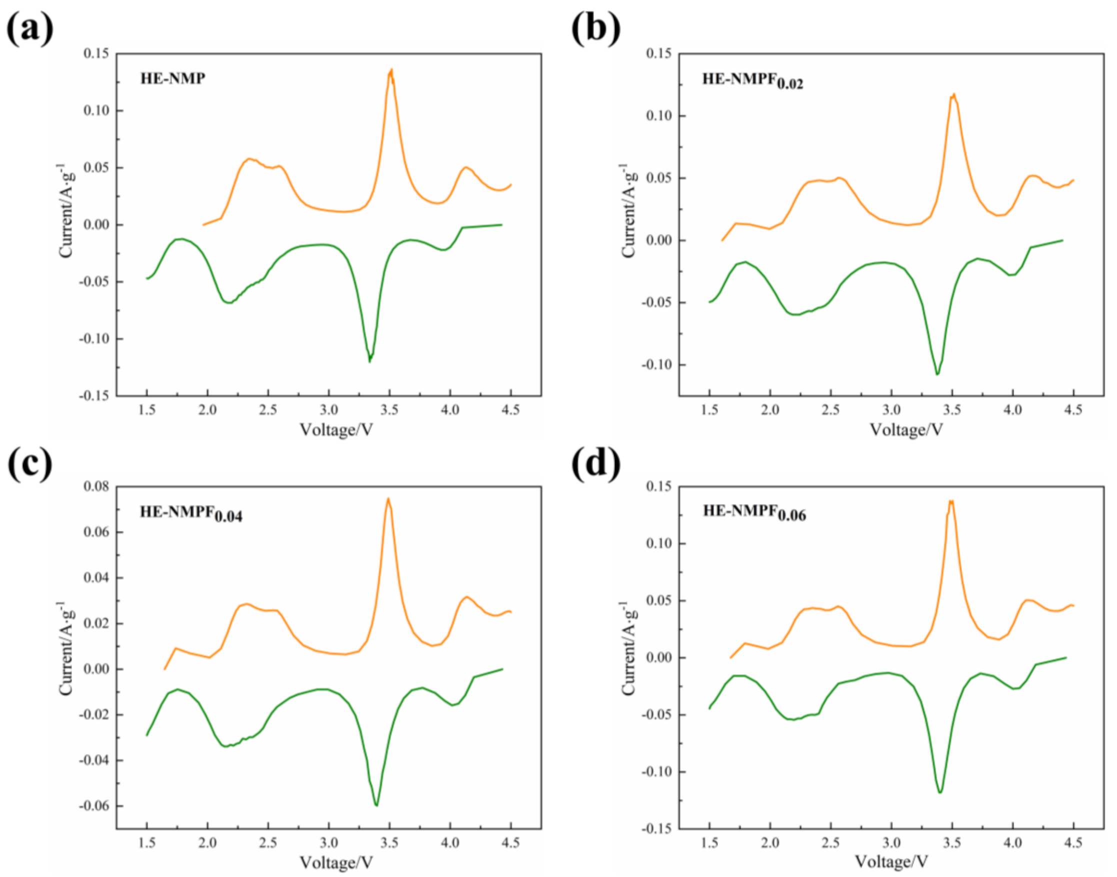

Fig. S7 Corresponded *dQ/dV* curves of (a) HE-NMP, (b) HE-NMPF$_{0.02}$, (c) HE-NMPF$_{0.04}$ and (d) HE-NMPF$_{0.06}$.

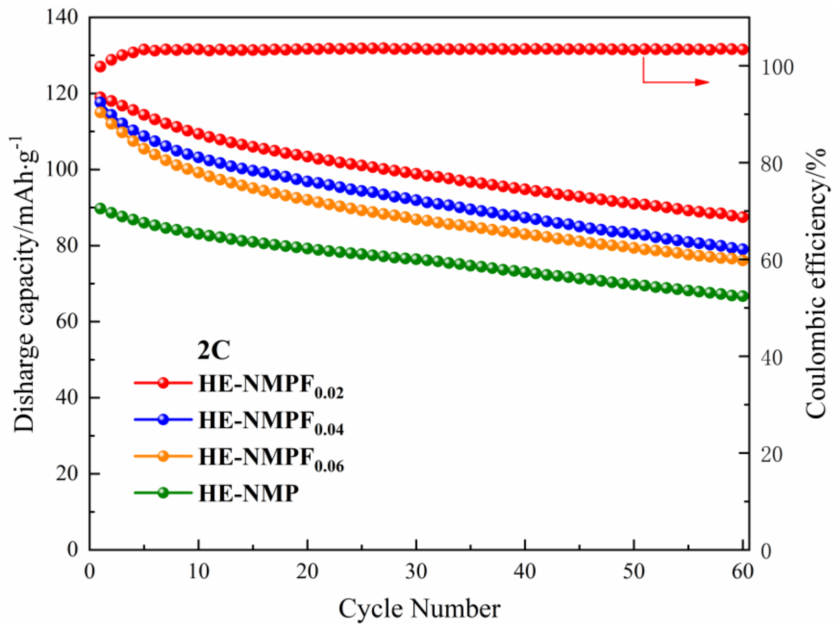

Fig. S8 Cycling performance at 2 C.

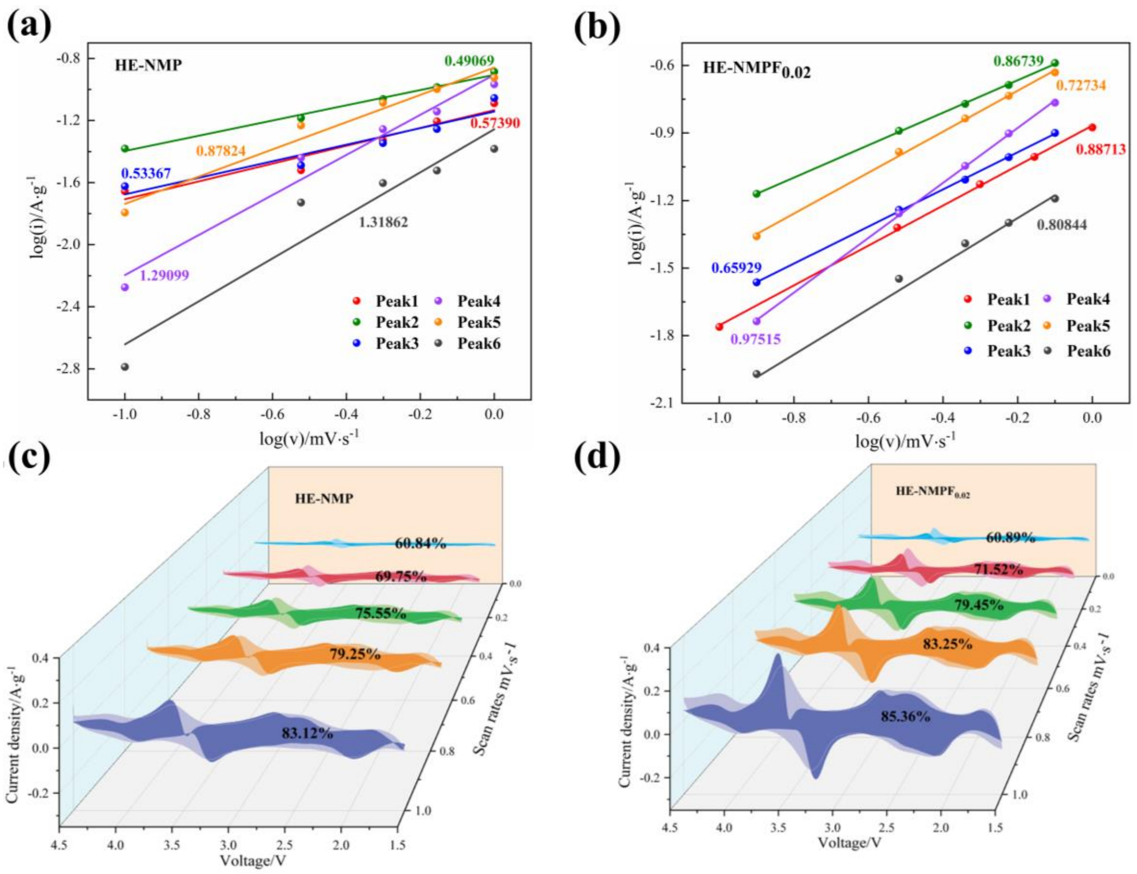

Fig. S9 (a, b) The log(i_p) versus log(v) curves and b values under different redox reactions; (c, d) Pseudocapacitance contribution percentage under different scan rates.

Table S1 Lattice parameters of all samples.

Sample	Lattice parameter a[Å]	Lattice parameter b[Å]	Lattice parameter c[Å]	Cell volume[$Å^3$]
HE-NMP	8.71868	8.71868	21.81623	1658.37
HE-$NMPF_{0.02}$	8.73557	8.73557	21.79696	1663.33
HE-$NMPF_{0.04}$	8.73545	8.73545	21.80180	1663.65
HE-$NMPF_{0.06}$	8.73528	8.73528	21.79744	1663.26

Table S2 Refined structure information of the HE-NMPF$_{0.02}$.

Crystal phase: trigonal, R-3c(S.G.); a=8.7355 Å, c=21.7970 Å, V=1663.33 Å^3						
Atom	x	y	z	Occ.	Uiso.	Wyckoff. Position
O1	0.15007	0.48239	0.07526	0.9983	0.03015	36f
O2	0.54815	0.83570	-0.02560	0.9983	0.03962	36f
P	-0.03376	0.33333	0.08333	0.9983	0.02238	18e
Na1	0.33333	0.66667	0.16667	1.2540	0.02862	6b
Na2	0.66667	0.98692	0.08333	0.7150	0.02894	18e
Mn	0.33333	0.66667	0.01799	0.1972	0.02062	12c
Fe	0.33333	0.66667	0.01799	0.1975	0.02062	12c
V	0.33333	0.66667	0.01799	0.2032	0.02062	12c
Ti	0.33333	0.66667	0.01799	0.2034	0.02062	12c
Cr	0.33333	0.66667	0.01799	0.1987	0.02062	12c
F1	0.15007	0.48239	0.07526	0.0017	0.03015	36f
F2	0.54815	0.83570	-0.02560	0.0017	0.03962	36f

Table S3 Energy dispersive spectroscopy (EDS) and inductively coupled plasma-optical emission spectroscopy (ICP-OES) data for HE-$NMPF_{0.02}$.

Element	EDS (Mass%)	ICP (Mass%)
Fe	5.34	4.14
Mn	5.98	4.17
V	5.46	3.97
Cr	5.48	4.01
Ti	5.25	3.91
F	3.04	—

Table S4 Specific surface area, total pore volume and average pore size of samples.

Sample	Surface area (m^2 g^{-1})	Pore volume (cm^3 g^{-1})	Pore Size (nm)
HE-NMP	1.6415	0.0118	13.8725
HE-$NMPF_{0.02}$	13.2662	0.0602	18.6465
HE-$NMPF_{0.04}$	10.4533	0.0290	17.4945
HE-$NMPF_{0.06}$	7.9565	0.0214	16.1358

Table S5 XPS peak positions of different orbitals for different elements.

	$2p_{1/2}$(eV)			$2p_{3/2}$(eV)		
	+2	+3	+4	+2	+3	+4
HE-NMP-Fe	724.81	727.28	-	711.68	715.18	-
HE-NMPF$_{0.02}$-Fe	724.70	727.01	-	711.40	715.02	-
HE-NMP-Mn	653.28	-	-	641.31	-	-
HE-NMPF$_{0.02}$-Mn	652.90	654.45	-	641.01	642.41	-
HE-NMP-V	-	523.68	-	-	517.37	-
HE-NMPF$_{0.02}$-V	-	523.35	-	-	517.00	-
HE-NMP-Cr	-	587.16	-	-	577.84	-
HE-NMPF$_{0.02}$-Cr	-	587.41	-	-	578.14	-
HE-NMP-Ti	-	464.71	465.88	-	458.80	459.92
HE-NMPF$_{0.02}$-Ti	-	464.98	-	-	459.04	-

Table S6 Data for calculating the voltage platform difference (ΔE).

Sample	charging	discharging	Voltage difference
HE-NMPF$_{0.02}$	3.52	2.52	1.00
HE-NMPF$_{0.04}$	3.57	2.37	1.20
HE-NMPF$_{0.06}$	3.74	2.31	1.43
HE-NMP	3.76	2.26	1.50

Table S7 Comparison of the electrochemical performance for NASICON-type cathodes as reported in recent literature.

Sample	Current density/A·g^{-1}	Cycle number	Specific capacity/mAh·g^{-1}	Ref.
$Na_3MnTi(PO_4)_3$	0.012	100	60	[1]
$Na_4MnCr(PO_4)_3$	0.56	600	47	[2]
$Na_3MnTi(PO_4)_3$	0.12	800	75	[3]
$Na_3V_2(PO_4)_2F_{2.5}O_{2.5}$	0.24	1000	75	[4]
$Na_xVMn_{0.75}Al_{0.25}(PO_4)_3$	0.12	347	83	[5]
$Na_4MnCr(PO_4)_3$	1.0	500	40	[6]
$Na_2VTi(PO_4)_3$@C	1.25	500	73	[7]
$Na_4MnV(PO_4)_3$	2.2	1000	54	[8]
$Na_4Fe_3(PO_4)_2(P_2O_7)$@C	2.4	1000	50	[9]
$Na_3Ti_{0.5}V_{0.5}(PO_3)_3N$	1.6	1000	53	[10]
$Na_3V_{1.9}(CaMgAlCrMn)_{0.01}(PO_4)_2F_3$	2.6	2000	80	[11]
$Na_3V(AlFeInGaCr)_{0.2}(PO_4)_3$	2.28	5000	71	[12]
$Na_3(TiVMnCrZr)_{0.4}(PO_4)_3$	0.1	100	33	[13]
$Na_{3.4}(FeMnVCrTi)_{0.4}(PO_4)_3$	0.75	1000	77	[14]
$Na_{3.4}(FeMnVCrTi)_{0.4}(PO_4)_{2.98}F_{0.02}$	3.0	1000	62	This work

Table S8 Fitted EIS curve data and calculated D_{Na+} data for the material.

Sample	Rs[Ω]	Rct[Ω]	D_{Na+} [cm^2 s^{-1}] [×10^{-12}]
HE-NMP	4.73	274	0.33
HE-NMPF$_{0.02}$	3.52	124	8.72
HE-NMPF$_{0.04}$	4.30	206	3.33
HE-NMPF$_{0.06}$	4.40	228	1.52

Reference

1. H. Gao, Y. Li, K. Park and J. B. Goodenough, Sodium Extraction from NASICON-Structured $Na_3MnTi(PO_4)_3$ through Mn(III)/Mn(II) and Mn(IV)/Mn(III) Redox Couples, *Chemistry of Materials*, 2016, **28**, 6553-6559.
2. J. Zhang, Y. Liu, X. Zhao, L. He, H. Liu, Y. Song, S. Sun, Q. Li, X. Xing and J. Chen, A Novel NASICON-Type $Na_4MnCr(PO_4)_3$ Demonstrating the Energy Density Record of Phosphate Cathodes for Sodium-Ion Batteries, *Advanced Materials*, 2020, **32**, 1906348.
3. T. Zhu, P. Hu, C. Cai, Z. Liu, G. Hu, Q. Kuang, L. Mai and L. Zhou, Dual carbon decorated $Na_3MnTi(PO_4)_3$: A high-energy-density cathode material for sodium-ion batteries, *Nano Energy*, 2020, **70**, 2211-2855.
4. W. Li, Z. Yao, S. Zhang, X. Wang, X. Xia, C. Gu and J. Tu, High-performance $Na_3V_2(PO_4)_2F_{2.5}O_{0.5}$ cathode: Hybrid reaction mechanism study via ex-situ XRD and sodium storage properties in solid-state batteries, *Chemical Engineering Journal*, 2021, **423**, 1385-8947.
5. S. Ghosh, N. Barman and P. Senguttuvan, Impact of Mg^{2+} and Al^{3+} Substitutions on the Structural and Electrochemical Properties of NASICON-$Na_xVMn_{0.75}M_{0.25}(PO_4)_3$ (M = Mg and Al) Cathodes for Sodium-Ion Batteries, *Small*, 2020, **16**, 2003973.
6. W. Zhang, H. Li, Z. Zhang, M. Xu, Y. Lai and S. L. Chou, Full Activation of Mn^{4+}/Mn^{3+} Redox in $Na_4MnCr(PO_4)_3$ as a High-Voltage and High-Rate Cathode Material for Sodium-Ion Batteries, *Small*, 2020, **16**, 2001524.

7. D. Wang, X. Bie, Q. Fu, D. Dixon, N. Bramnik, Y.-S. Hu, F. Fauth, Y. Wei, H. Ehrenberg, G. Chen and F. Du, Sodium vanadium titanium phosphate electrode for symmetric sodium-ion batteries with high power and long lifespan, *Nature Communications*, 2017, **8**, 15888.

8. H. Li, T. Jin, X. Chen, Y. Lai, Z. Zhang, W. Bao and L. Jiao, Rational Architecture Design Enables Superior Na Storage in Greener NASICON-$Na_4MnV(PO_4)_3$ Cathode, *Advanced Energy Materials*, 2018, **8**, 1801418.

9. M. Chen, W. Hua, J. Xiao, D. Cortie, W. Chen, E. Wang, Z. Hu, Q. Gu, X. Wang, S. Indris, S.-L. Chou and S.-X. Dou, NASICON-type air-stable and all-climate cathode for sodium-ion batteries with low cost and high-power density, *Nature Communications*, 2019, **10**, 1480.

10. M. Chen, J. Xiao, W. Hua, Z. Hu, W. Wang, Q. Gu, Y. Tang, S. L. Chou, H. K. Liu and S. X. Dou, A Cation and Anion Dual Doping Strategy for the Elevation of Titanium Redox Potential for High-Power Sodium-Ion Batteries, *Angewandte Chemie International Edition*, 2020, **59**, 12076-12083.

11. Z. Y. Gu, J. Z. Guo, J. M. Cao, X. T. Wang, X. X. Zhao, X. Y. Zheng, W. H. Li, Z. H. Sun, H. J. Liang and X. L. Wu, An Advanced High-Entropy Fluorophosphate Cathode for Sodium-Ion Batteries with Increased Working Voltage and Energy Density, *Advanced Materials*, 2022, **34**, 2110108.

12. M. Li, C. Sun, Q. Ni, Z. Sun, Y. Liu, Y. Li, L. Li, H. Jin and Y. Zhao, High Entropy Enabling the Reversible Redox Reaction of V^{4+}/V^{5+} Couple in NASICON-Type

Sodium Ion Cathode, *Advanced Energy Materials*, 2023, **13**, 2203971.

13. B. Wu, G. Hou, E. Kovalska, V. Mazanek, P. Marvan, L. Liao, L. Dekanovsky, D. Sedmidubsky, I. Marek, C. Hervoches and Z. Sofer, High-Entropy NASICON Phosphates ($Na_3M_2(PO_4)_3$ and $NaMPO_4O_x$, M = Ti, V, Mn, Cr, and Zr) for Sodium Electrochemistry, *Inorganic Chemistry*, 2022, **61**, 4092-4101.
14. H. Li, M. Xu, H. Long, J. Zheng, L. Zhang, S. Li, C. Guan, Y. Lai and Z. Zhang, Stabilization of Multicationic Redox Chemistry in Polyanionic Cathode by Increasing Entropy, *Advanced Science*, 2022, **9**, 2202082.